nature catalysis

SUPPLEMENTARY INFORMATION

https://doi.org/10.1038/s41929-019-0380-x

In the format provided by the authors and unedited.

Constraining CO coverage on copper promotes high-efficiency ethylene electroproduction

Jun Li[1,2,5], Ziyun Wang[2,5], Christopher McCallum[1,5], Yi Xu[1], Fengwang Li[2], Yuhang Wang[2], Christine M. Gabardo[1], Cao-Thang Dinh[2], Tao-Tao Zhuang[2], Liang Wang[3], Jane Y. Howe[4], Yang Ren[3], Edward H. Sargent[2]* and David Sinton[1]*

[1]Department of Mechanical and Industrial Engineering, University of Toronto, Toronto, Ontario, Canada. [2]Department of Electrical and Computer Engineering, University of Toronto, Toronto, Ontario, Canada. [3]X-ray Science Division, Argonne National Laboratory, Lemont, IL, USA. [4]Hitachi High Technologies America, Clarksburg, MD, USA. [5]These authors contributed equally: Jun Li, Ziyun Wang and Christopher McCallum
*e-mail: ted.sargent@utoronto.ca; sinton@mie.utoronto.ca

Constraining CO coverage on copper promotes high-efficiency ethylene electroproduction

Jun Li[1,2†], Ziyun Wang[2†], Christopher McCallum[1†], Yi Xu[1], Fengwang Li[2], Yuhang Wang[2], Christine Gabardo[1], Cao-Thang Dinh[2], Tao-Tao Zhuang[2], Liang Wang[3], Jane Y. Howe[4], Yang Ren[3], Edward H. Sargent[2] & David Sinton[1]**

[1]*Department of Mechanical and Industrial Engineering, University of Toronto, 5 King's College Road, Toronto, Ontario, M5S 3G8, Canada.*

[2]*Department of Electrical and Computer Engineering, University of Toronto, 10 King's College Road, Toronto, Ontario, M5S 3G4, Canada.*

[3]*Advanced Photon Source, Argonne National Laboratory, Lemont, Illinois, 60439, United States*

[4]*Hitachi High Technologies America, Inc., 22610 Gateway Center Drive, Suite 100, Clarksburg, Maryland 20871, USA*

[†]*These authors contributed equally: Jun Li, Ziyun Wang and Christopher McCallum.*
**Corresponding email: ted.sargent@utoronto.ca; sinton@mie.utoronto.ca*

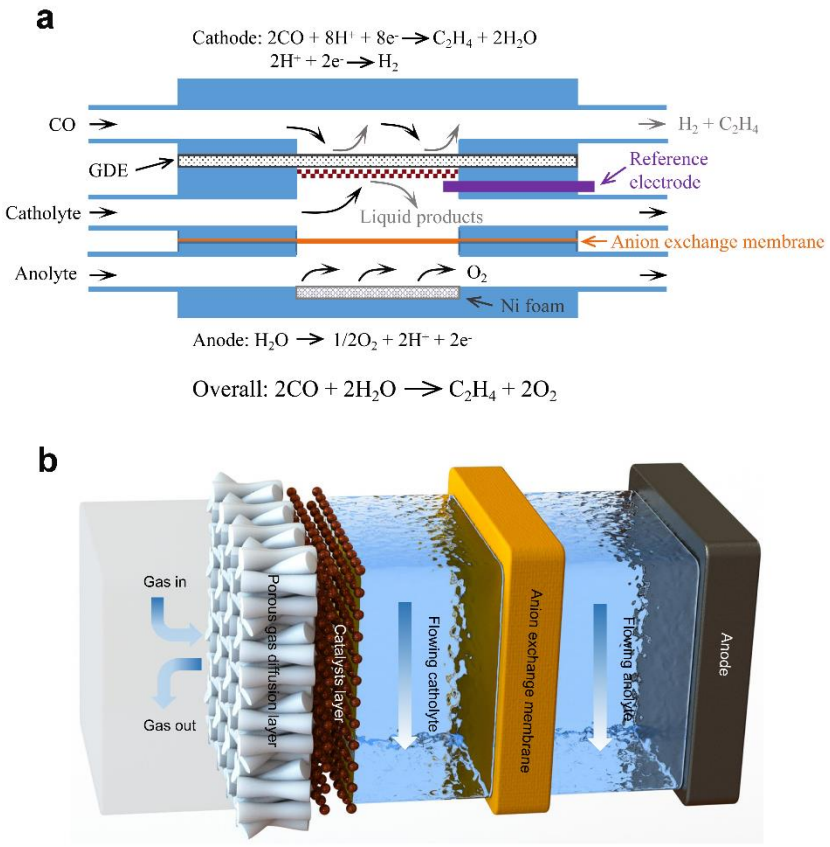

Supplementary Fig. 1. Schematic illustrations of flow cell electrolyzer. a, A two-dimensional cross-section view. **b,** A three-dimensional layout.

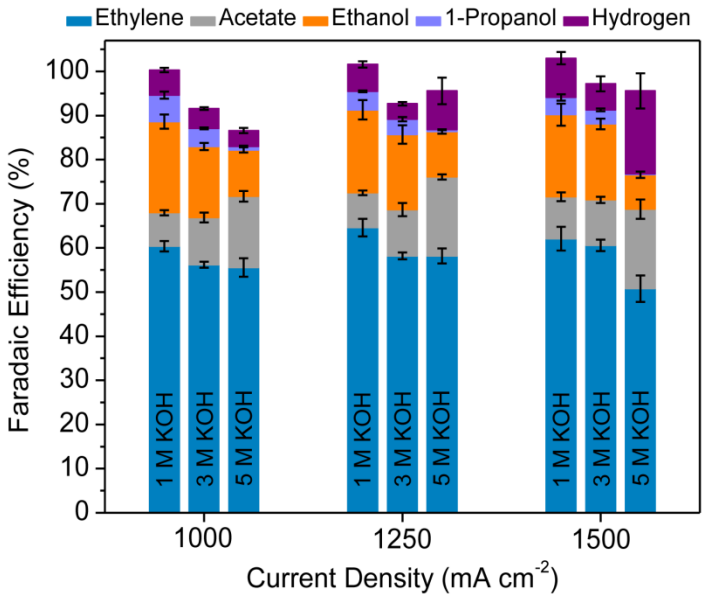

Supplementary Fig. 2. Faradaic efficiencies of all products from CO reduction in 1 M, 3 M and 5 M KOH at selected current densities. Error bars are means ± SD (n = 3 replicates).

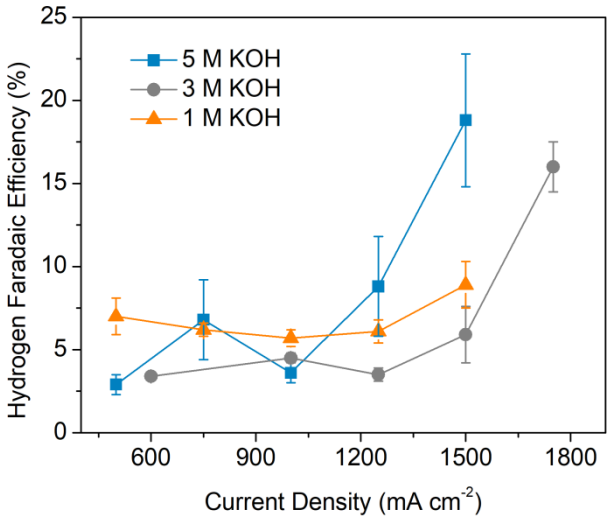

Supplementary Fig. 3. Hydrogen Faradaic efficiencies at various KOH concentrations as a function of applied current density. Error bars are means ± SD (n = 3 replicates).

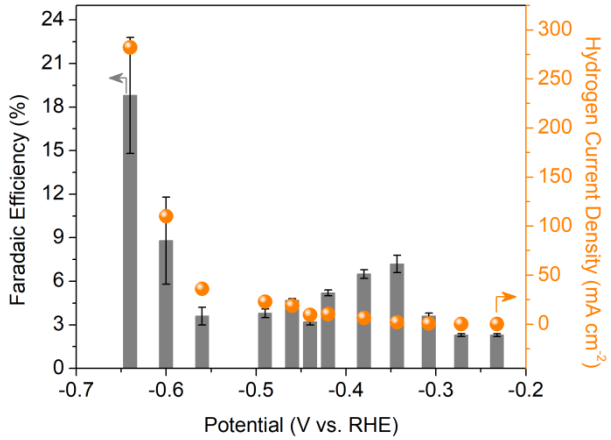

Supplementary Fig. 4. Hydrogen Faradaic efficiency and partial current density from CO reduction in 5 M KOH as a function of applied potential. Error bars are means ± SD (n = 3 replicates).

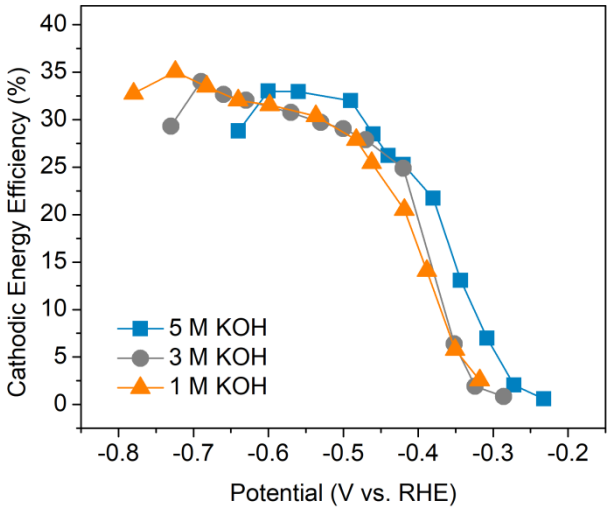

Supplementary Fig. 5. Cathodic energy efficiencies for ethylene electroproduction from CO reduction at various KOH concentrations as a function of applied potential.

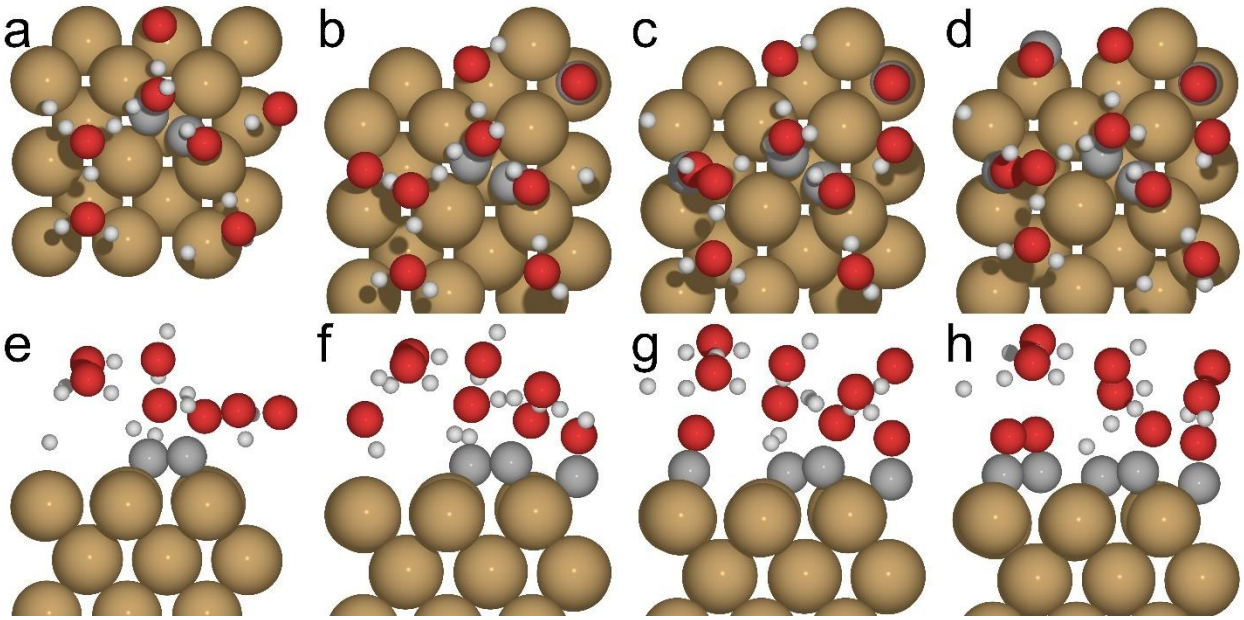

Supplementary Fig. 6. The geometries of key intermediates branching ethylene and ethanol, *CHCOH, on Cu(100) with solvent molecules at different CO coverage: **a** and **e** at 0 ML, **b** and **f** at 1/9 ML, **c** and **g** at 2/9 ML, **d** and **h** at 3/9 ML. Yellow, red, grey, and white balls stand for copper, oxygen, carbon, and hydrogen atoms, respectively. These notations are used throughout this document.

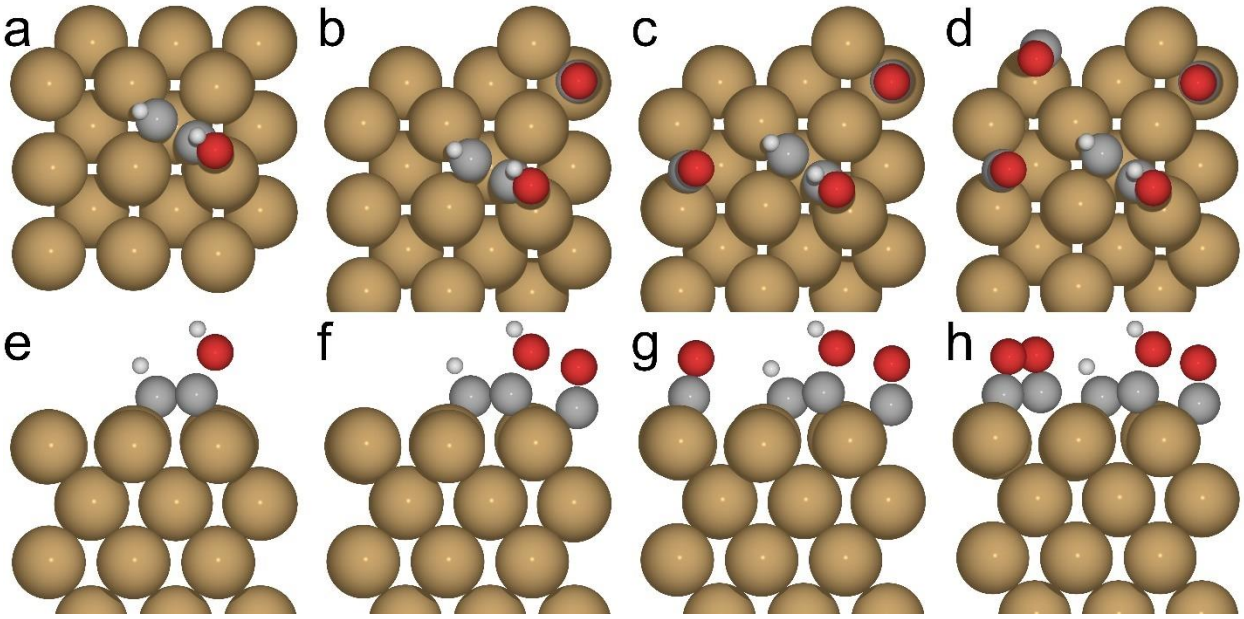

Supplementary Fig. 7. The geometries of key intermediates branching ethylene and ethanol, *CHCOH, on Cu(100) without solvent molecules at different CO coverage: **a** and **e** at 0 ML, **b** and **f** at 1/9 ML, **c** and **g** at 2/9 ML, **d** and **h** at 3/9 ML.

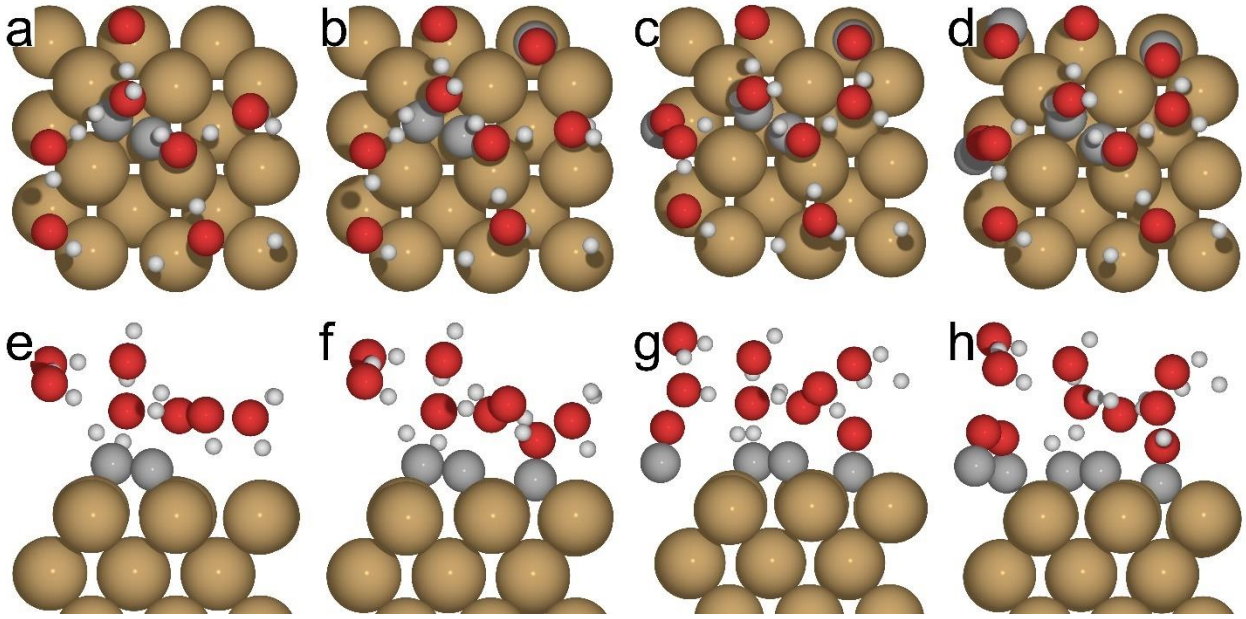

Supplementary Fig. 8. The transition state geometries of *CHCOH dehydroxylation to *CCH on Cu(100) with solvent molecules at different CO coverage: **a** and **e** at 0 ML, **b** and **f** at 1/9 ML, **c** and **g** at 2/9 ML, **d** and **h** at 3/9 ML.

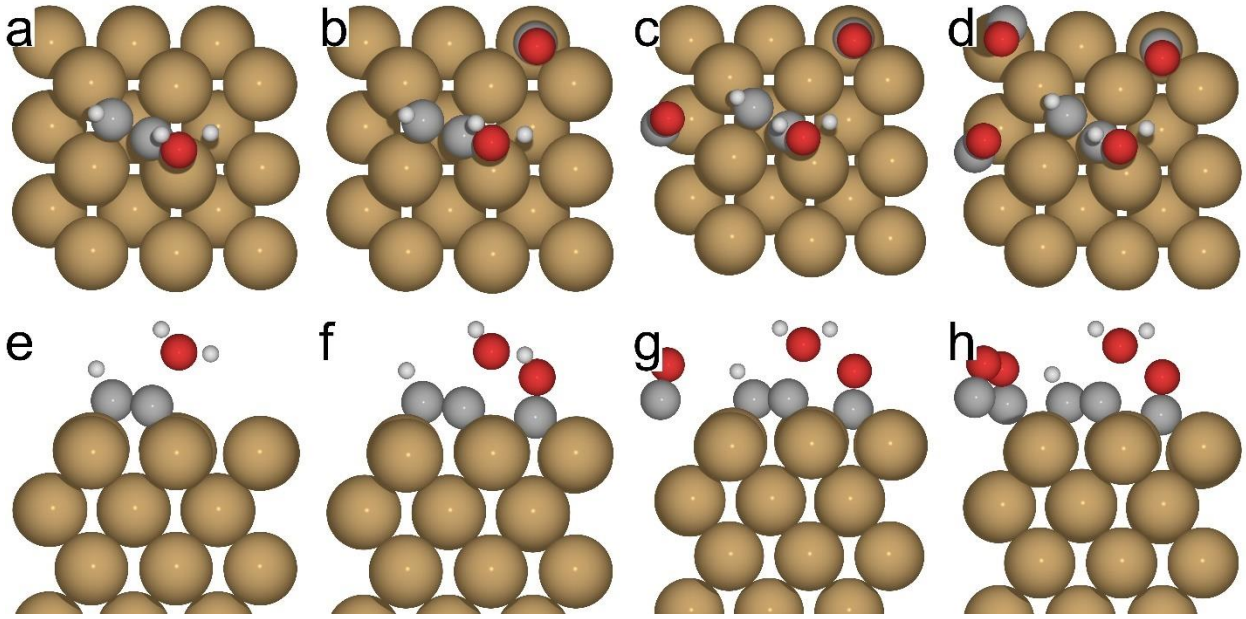

Supplementary Fig. 9. The transition state geometries of *CHCOH dehydroxylation to *CCH on Cu(100) without solvent molecules at different CO coverage: **a** and **e** at 0 ML, **b** and **f** at 1/9 ML, **c** and **g** at 2/9 ML, **d** and **h** at 3/9 ML.

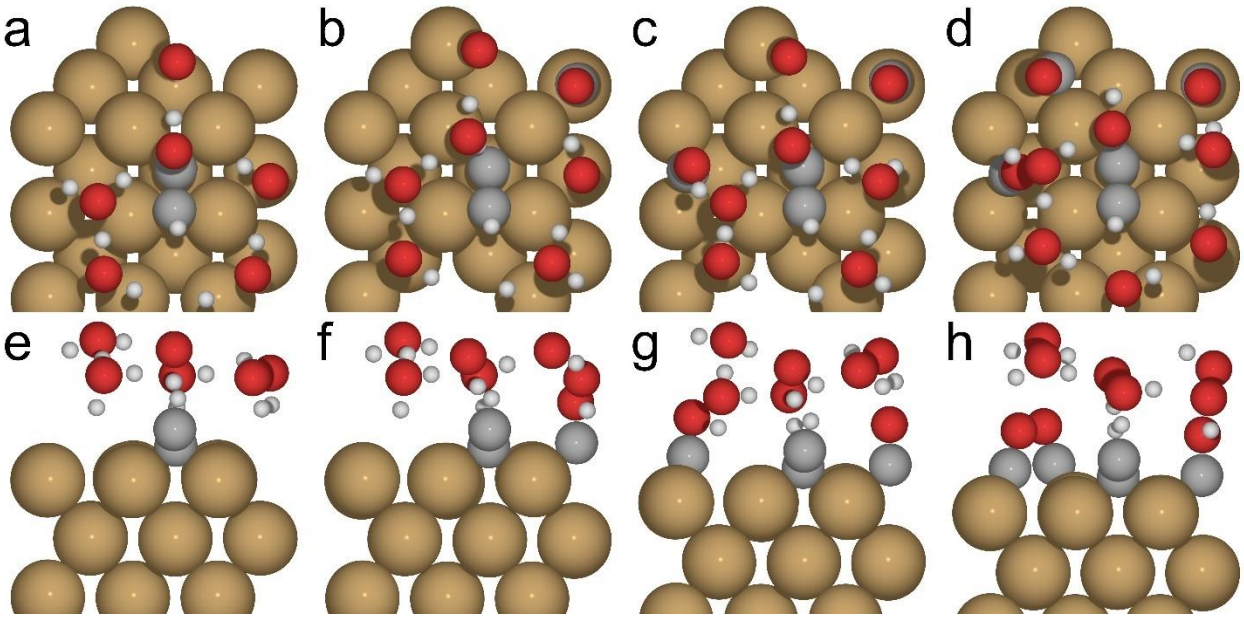

Supplementary Fig. 10. The final state geometries of *CHCOH dehydroxylation to *CCH on Cu(100) with solvent molecules at different CO coverage: **a** and **e** at 0 ML, **b** and **f** at 1/9 ML, **c** and **g** at 2/9 ML, **d** and **h** at 3/9 ML.

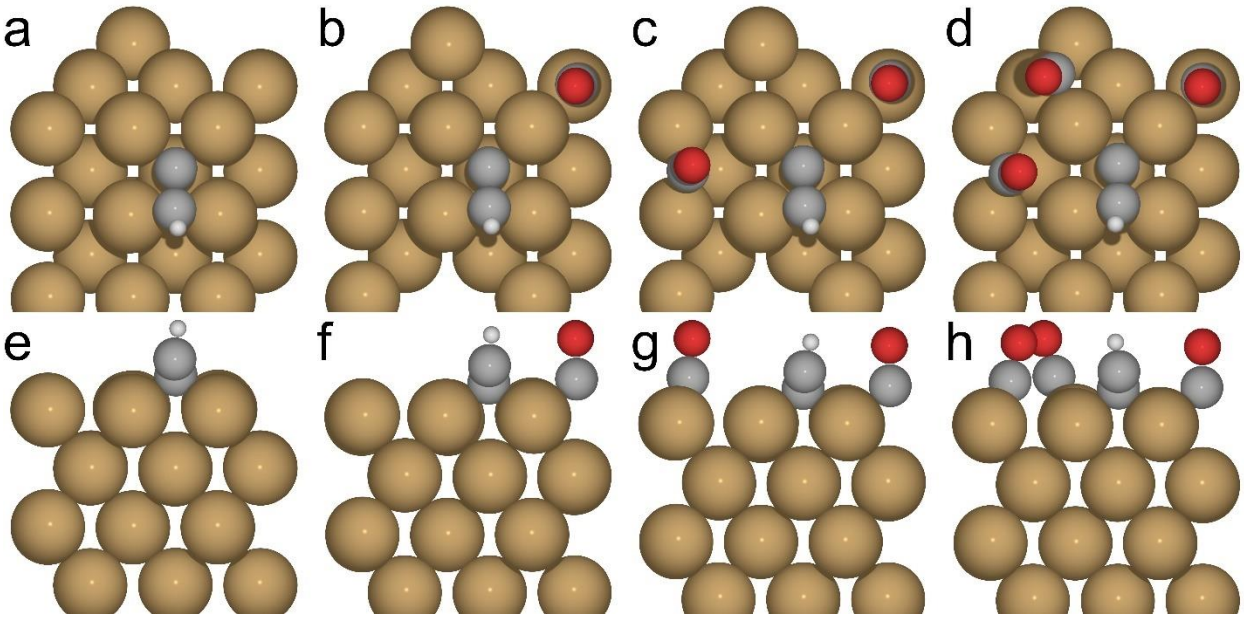

Supplementary Fig. 11. The final state geometries of *CHCOH dehydroxylation to *CCH on Cu(100) without solvent molecules at different CO coverage: **a** and **e** at 0 ML, **b** and **f** at 1/9 ML, **c** and **g** at 2/9 ML, **d** and **h** at 3/9 ML.

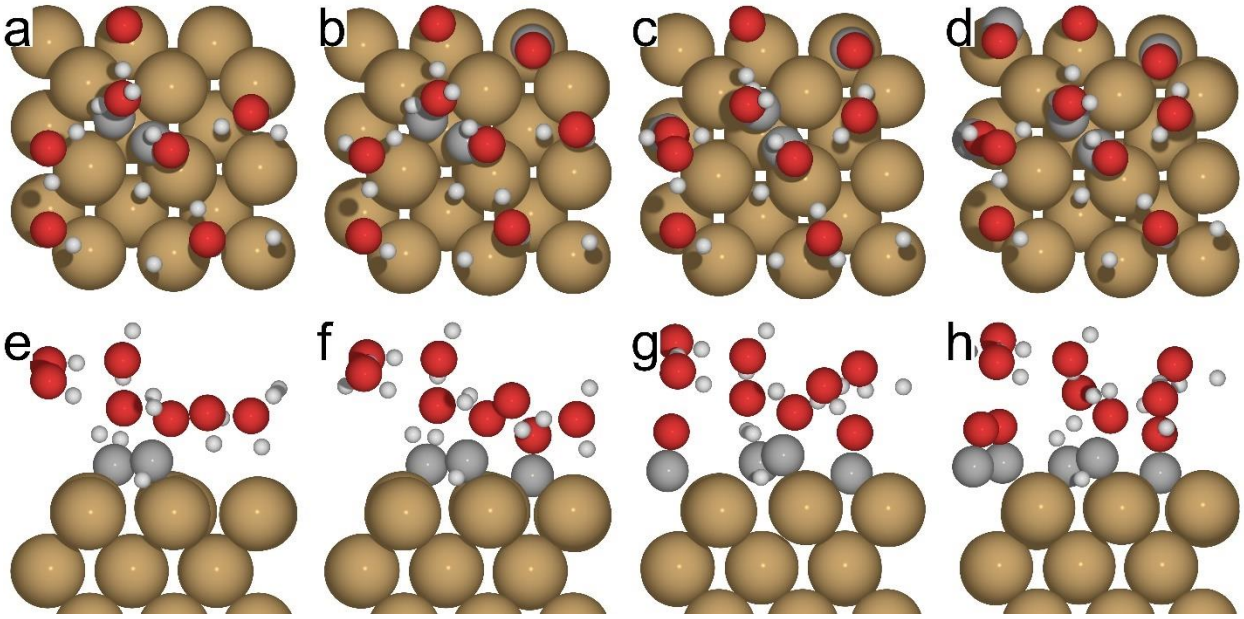

Supplementary Fig. 12. The transition state geometries of *CHCOH hydrogenation to *CHCHOH on Cu(100) with solvent molecules at different CO coverage: **a** and **e** at 0 ML, **b** and **f** at 1/9 ML, **c** and **g** at 2/9 ML, **d** and **h** at 3/9 ML.

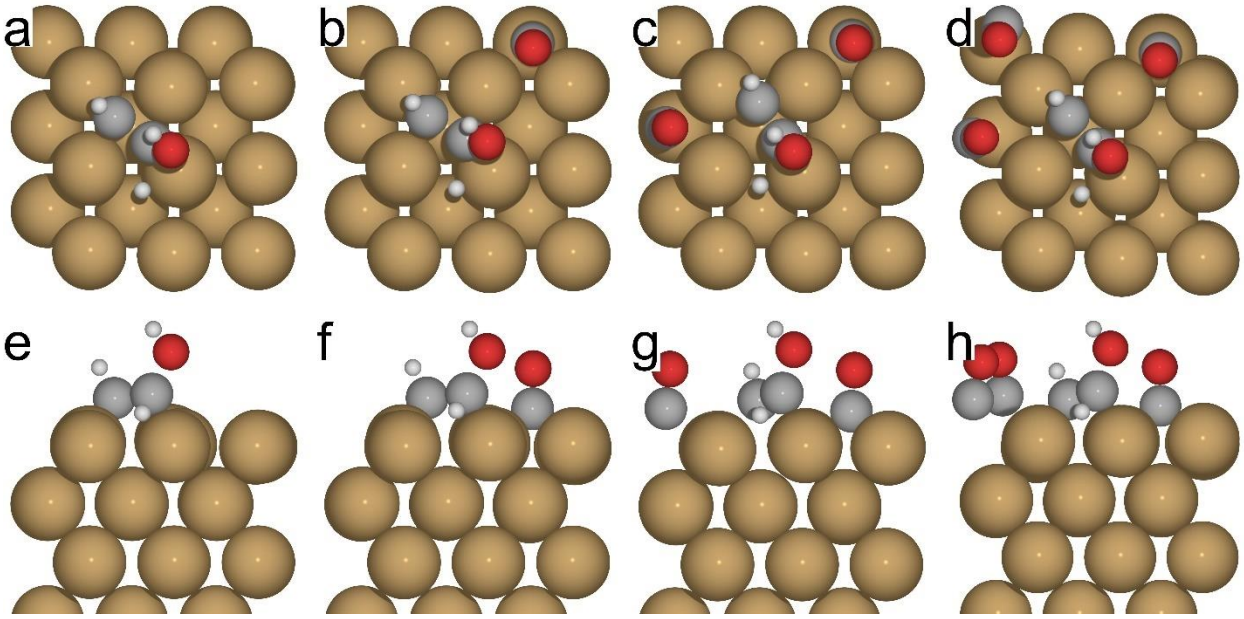

Supplementary Fig. 13. The transition state geometries of *CHCOH hydrogenation to *CHCHOH on Cu(100) without solvent molecules at different CO coverage: **a** and **e** at 0 ML, **b** and **f** at 1/9 ML, **c** and **g** at 2/9 ML, **d** and **h** at 3/9 ML.

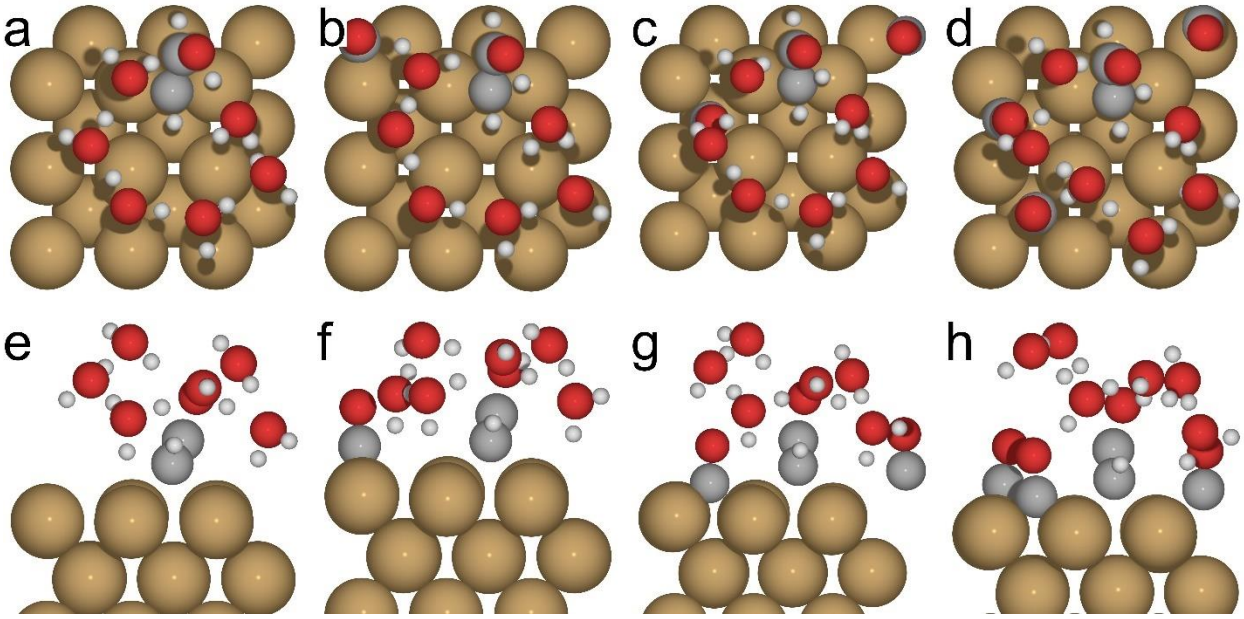

Supplementary Fig. 14. The final state geometries of *CHCOH hydrogenation to *CHCHOH on Cu(100) with solvent molecules at different CO coverage: **a** and **e** at 0 ML, **b** and **f** at 1/9 ML, **c** and **g** at 2/9 ML, **d** and **h** at 3/9 ML.

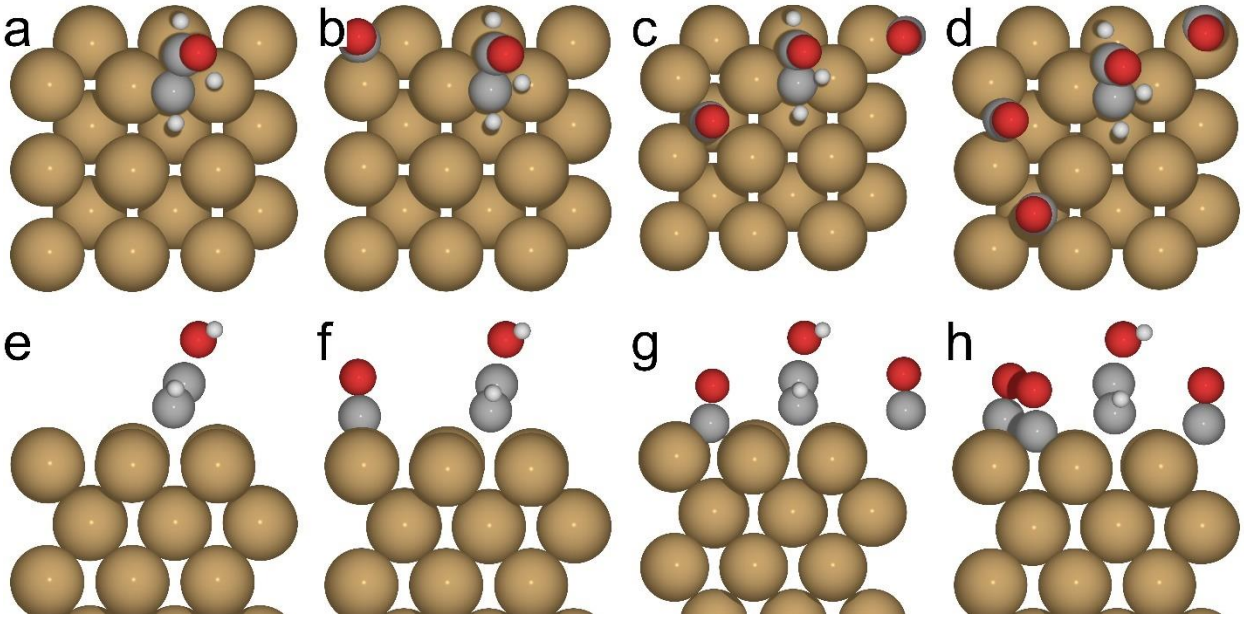

Supplementary Fig. 15. The final state geometries of *CHCOH hydrogenation to *CHCHOH on Cu(100) without solvent molecules at different CO coverage: **a** and **e** at 0 ML, **b** and **f** at 1/9 ML, **c** and **g** at 2/9 ML, **d** and **h** at 3/9 ML.

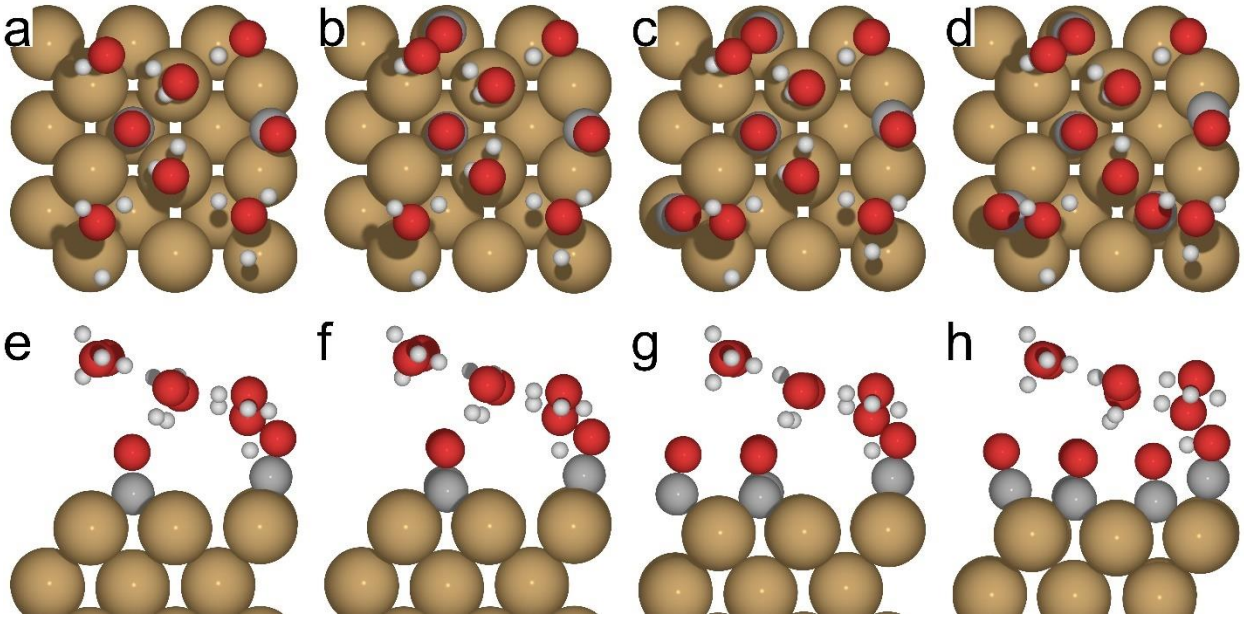

Supplementary Fig. 16. The initial state geometries of CO dimerization on Cu(100) with solvent molecules at different CO coverage: **a** and **e** at 2/9 ML, **b** and **f** at 3/9 ML, **c** and **g** at 4/9 ML, **d** and **h** at 5/9 ML.

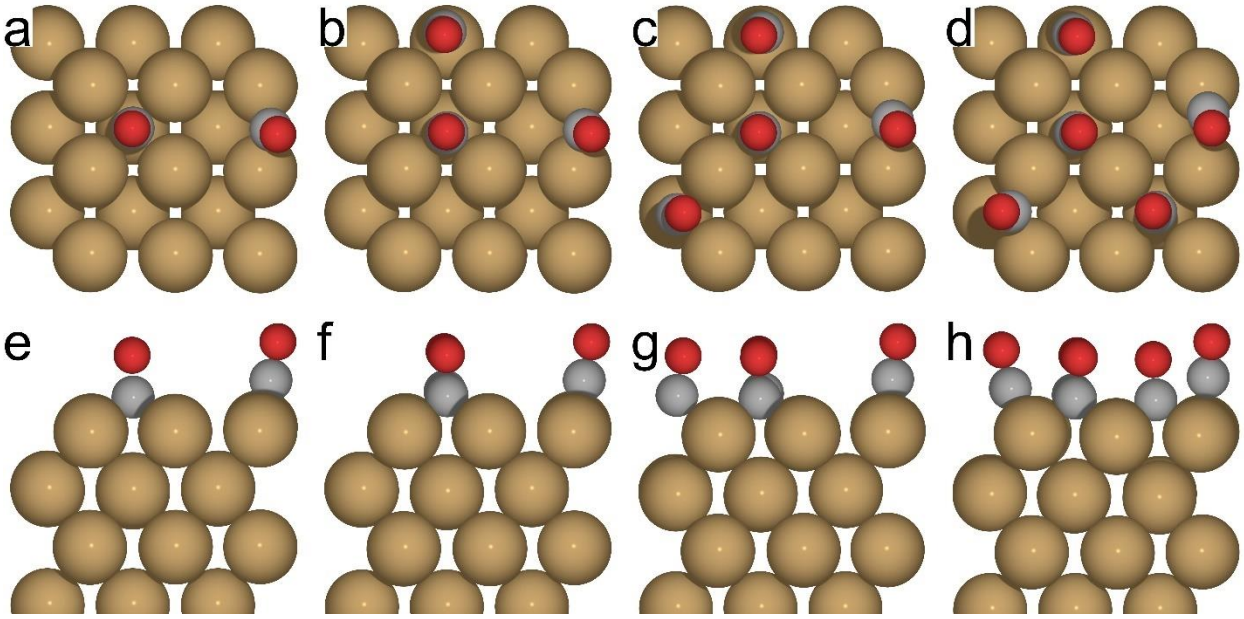

Supplementary Fig. 17. The initial state geometries of CO dimerization on Cu(100) without solvent molecules at different CO coverage: **a** and **e** at 2/9 ML, **b** and **f** at 3/9 ML, **c** and **g** at 4/9 ML, **d** and **h** at 5/9 ML.

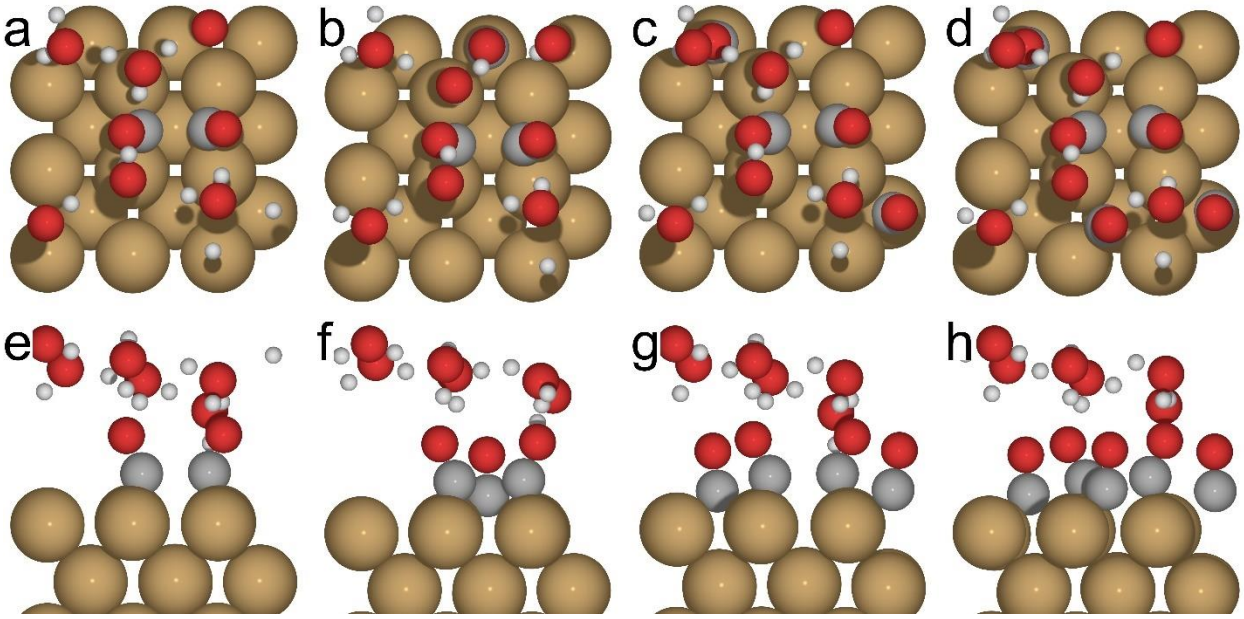

Supplementary Fig. 18. The transition state geometries of CO dimerization on Cu(100) with solvent molecules at different CO coverage: **a** and **e** at 2/9 ML, **b** and **f** at 3/9 ML, **c** and **g** at 4/9 ML, **d** and **h** at 5/9 ML.

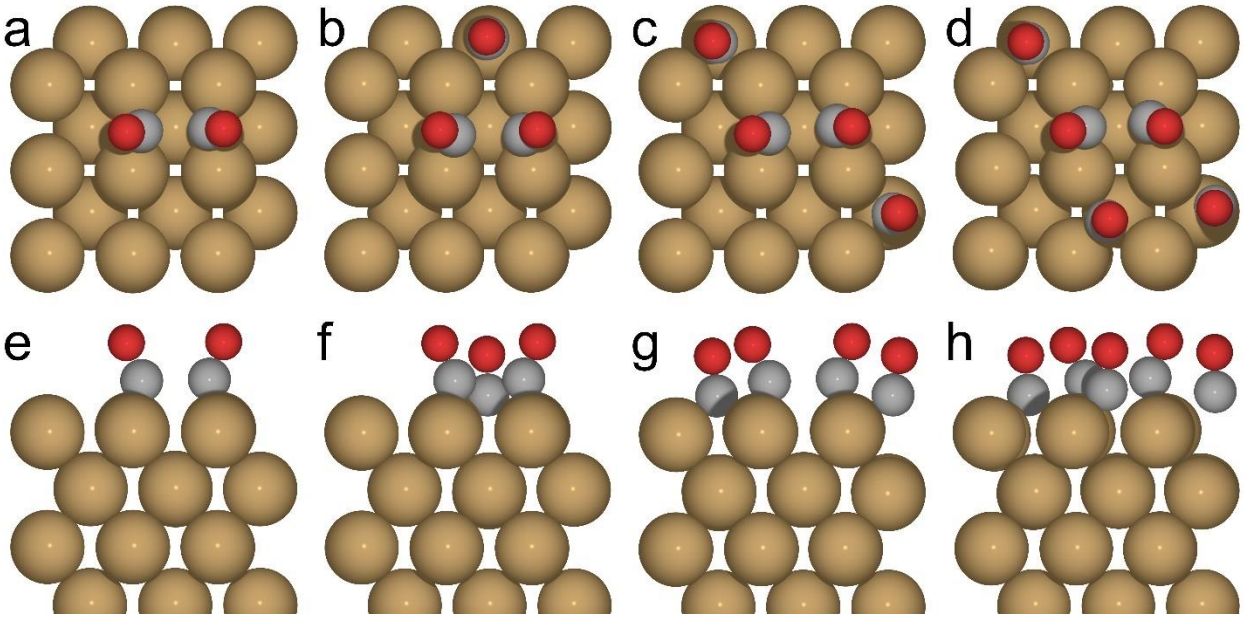

Supplementary Fig. 19. The transition state geometries of CO dimerization on Cu(100) without solvent molecules at different CO coverage: **a** and **e** at 2/9 ML, **b** and **f** at 3/9 ML, **c** and **g** at 4/9 ML, **d** and **h** at 5/9 ML.

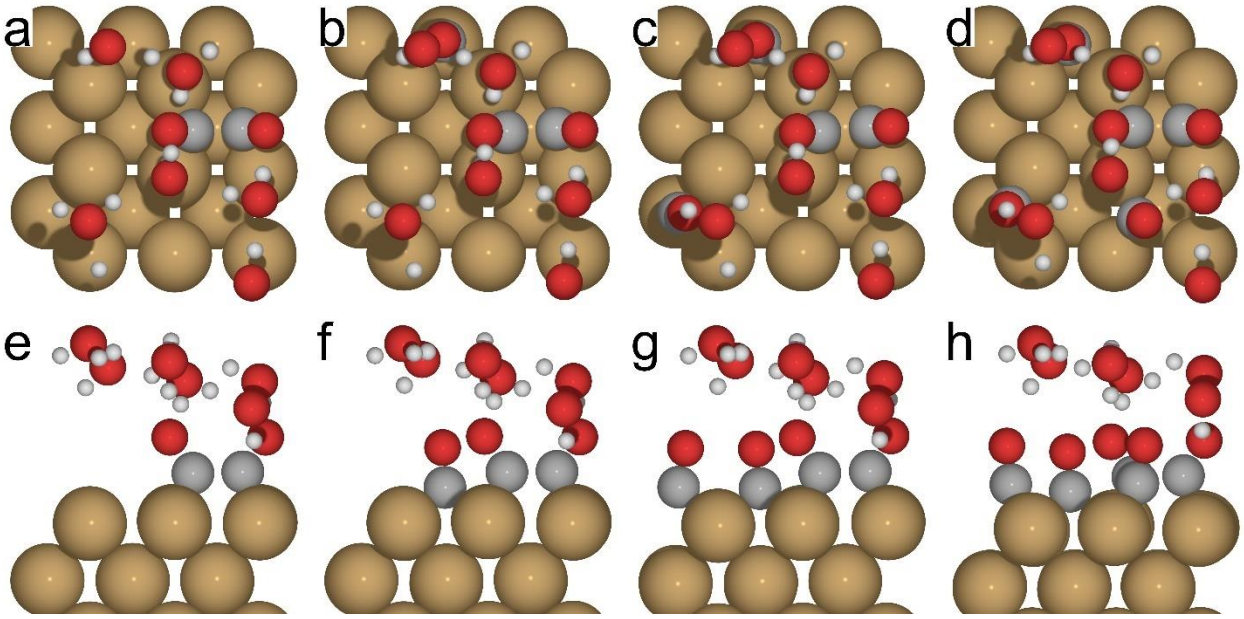

Supplementary Fig. 20. The final state geometries of CO dimerization on Cu(100) with solvent molecules at different CO coverage: **a** and **e** at 2/9 ML, **b** and **f** at 3/9 ML, **c** and **g** at 4/9 ML, **d** and **h** at 5/9 ML.

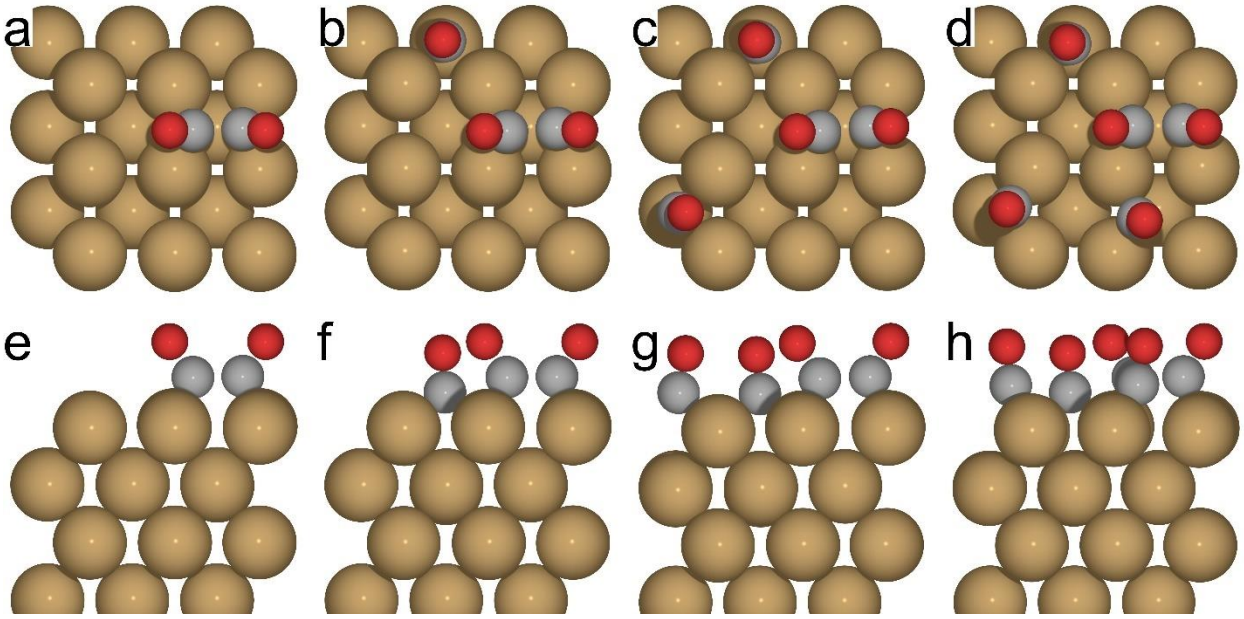

Supplementary Fig. 21. The final state geometries of CO dimerization on Cu(100) without solvent molecules at different CO coverage: **a** and **e** at 2/9 ML, **b** and **f** at 3/9 ML, **c** and **g** at 4/9 ML, **d** and **h** at 5/9 ML.

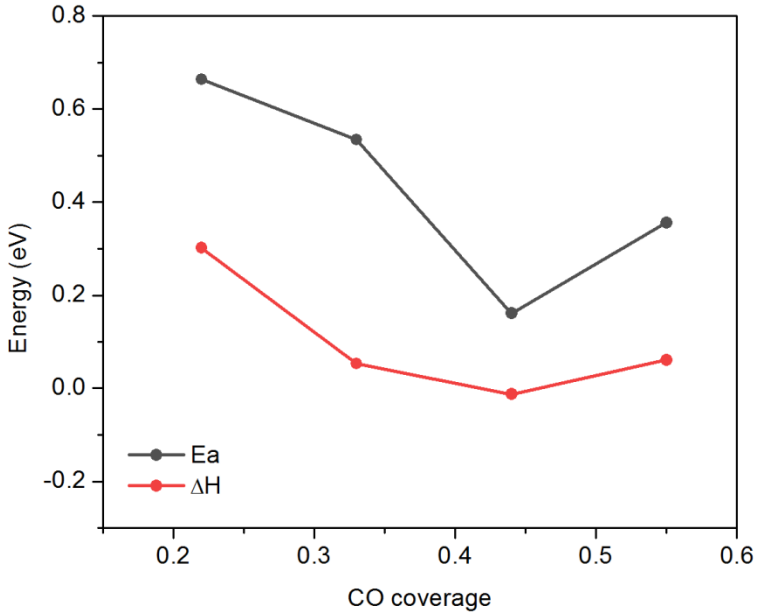

Supplementary Fig. 22. The reaction barrier and enthalpy change of CO dimerization on Cu(100) at different CO coverage.

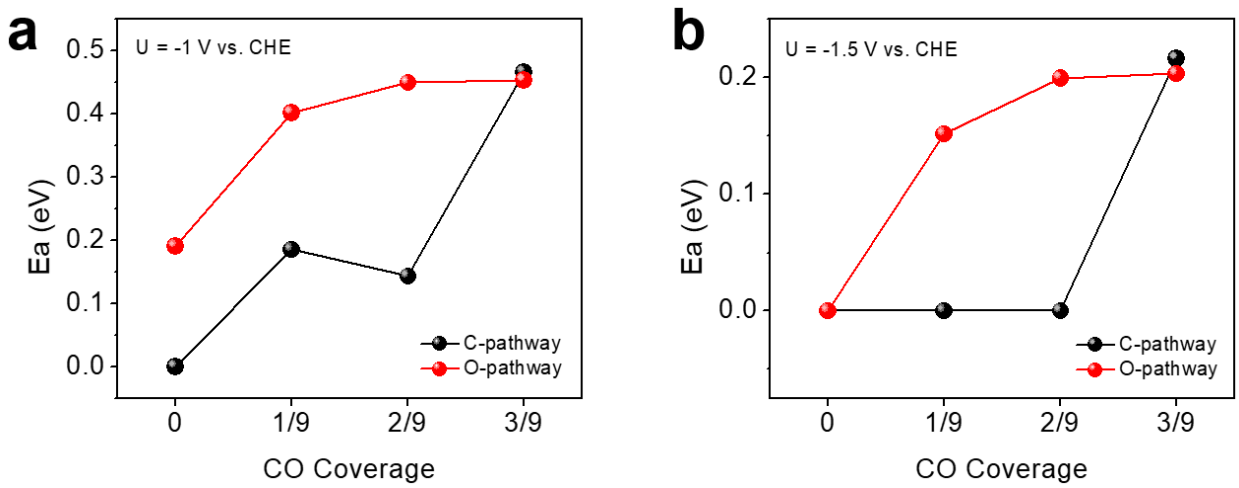

Supplementary Fig. 23. a, b, Activation energy as a function of coverage for the C- and O-pathways, at -1 V (**a**) and -1.5 V (**b**) versus the computational hydrogen electrode (CHE = SHE).

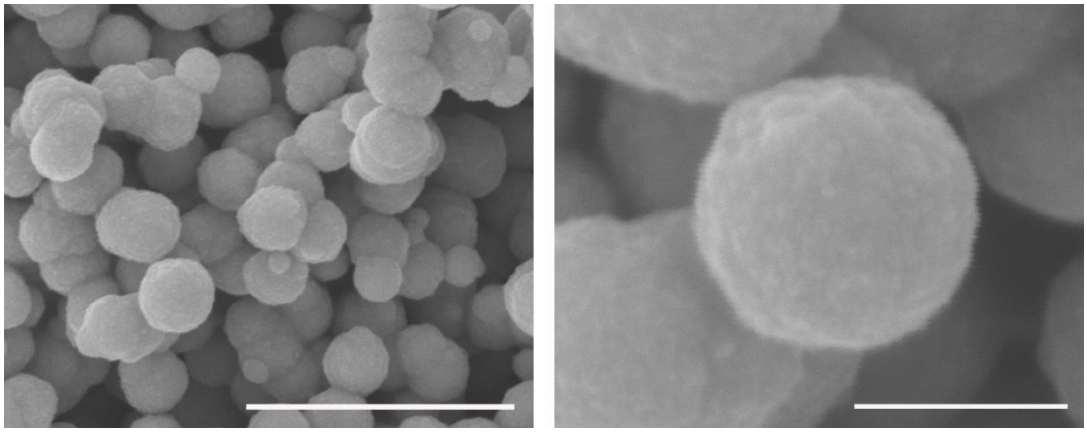

Supplementary Fig. 24. SEM images of oxide pre-catalysts. The scale bars are 1 μm on the left and 200 nm on the right.

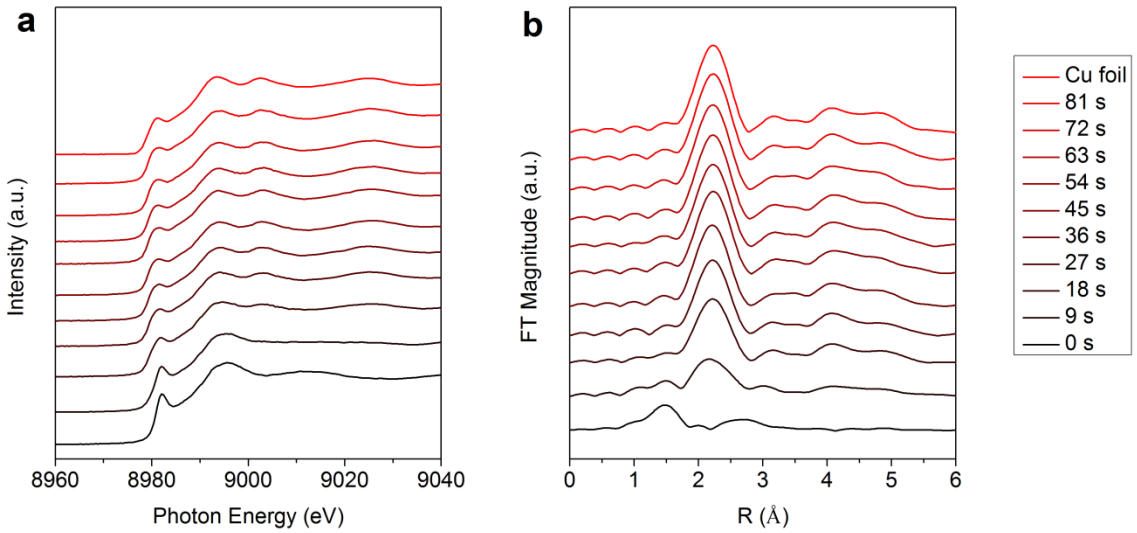

Supplementary Fig. 25. Operando X-ray absorption spectroscopy (XAS) analysis. a, A real-time Cu K-edge XAS tracking of the oxide reduction process. Each spectrum was collected at a time scale of 9 s. **b,** A Fourier Transform (FT) process of XAS spectra in (**a**). Ex-situ Cu foil spectra are included for comparison. The oxide reduction completes in ~1 min during CORR in 1 M KOH with the application of a constant current density of 120 mA cm^{-2}.

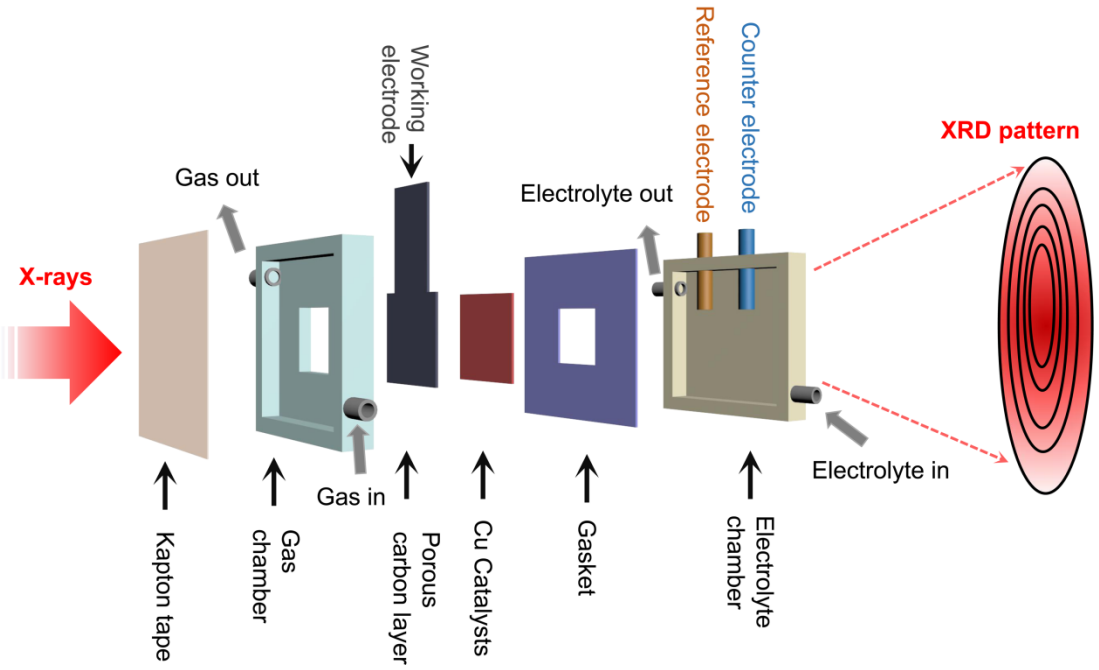

Supplementary Fig. 26. A schematic view of a flow cell design for high-resolution in operando X-ray diffraction test.

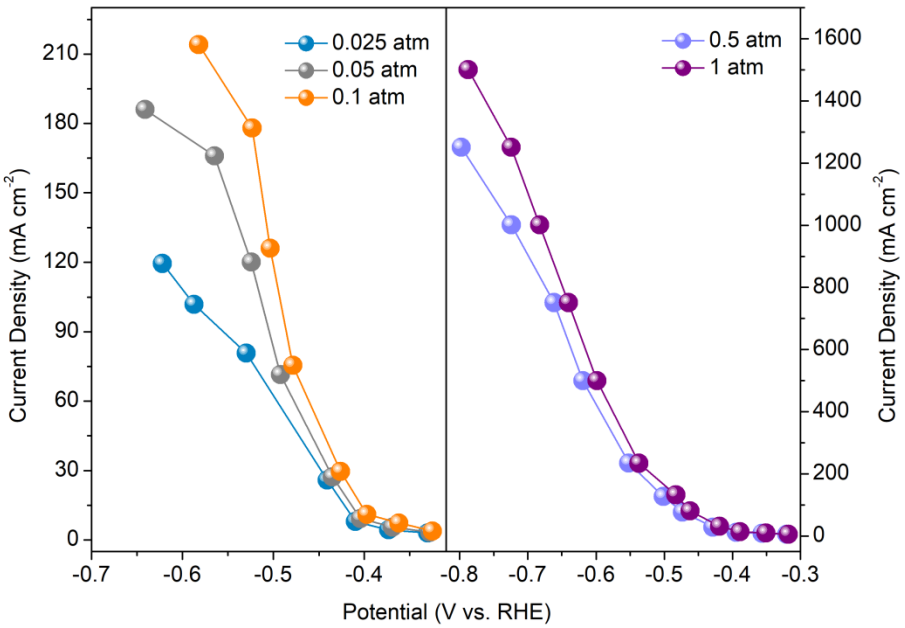

Supplementary Fig. 27. Total current densities of CORR at various CO pressures as a function of applied potential in 1 M KOH.

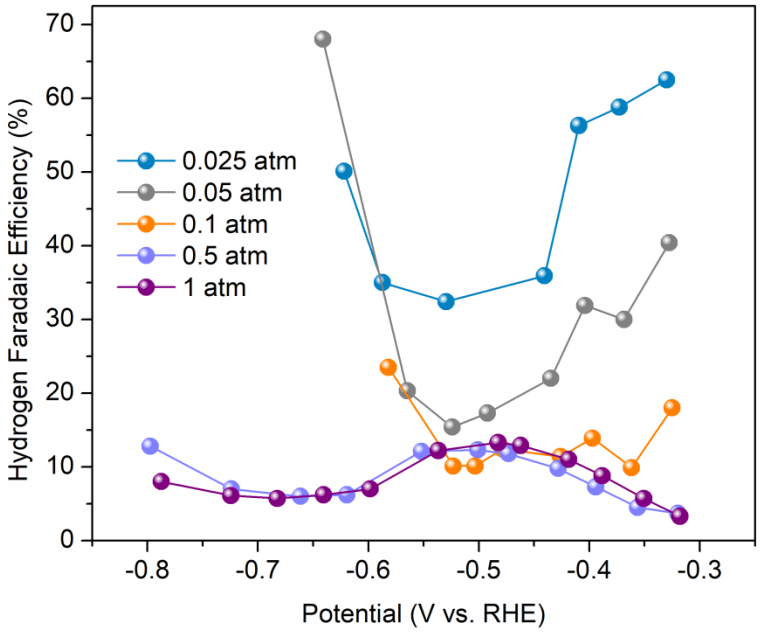

Supplementary Fig. 28. Hydrogen Faradaic efficiencies at various CO pressures as a function of applied potential in 1 M KOH.

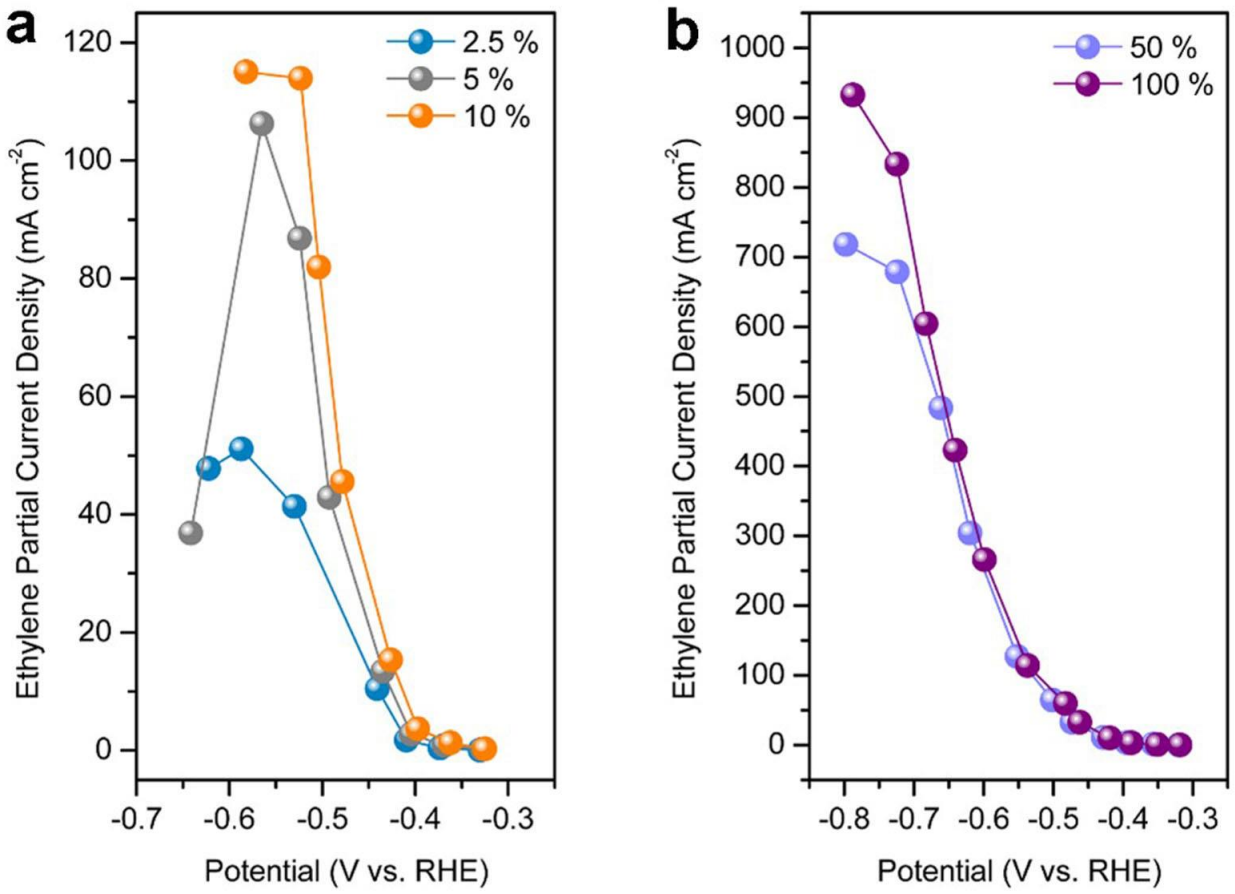

Supplementary Fig. 29. Ethylene partial current densities at various CO pressures as a function of applied potential in 1 M KOH.

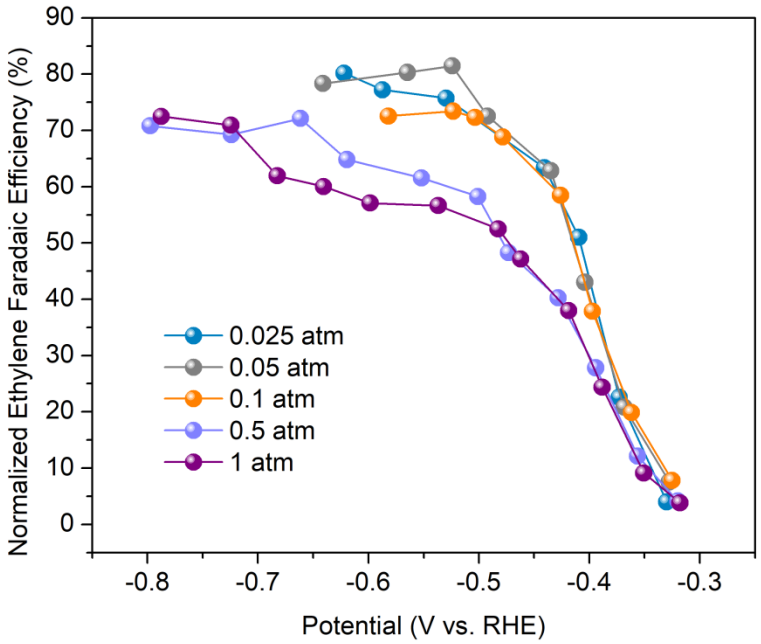

Supplementary Fig. 30. Normalized $FE_{ethylene}$ at different CO pressures as a function of applied potential in 1 M KOH.

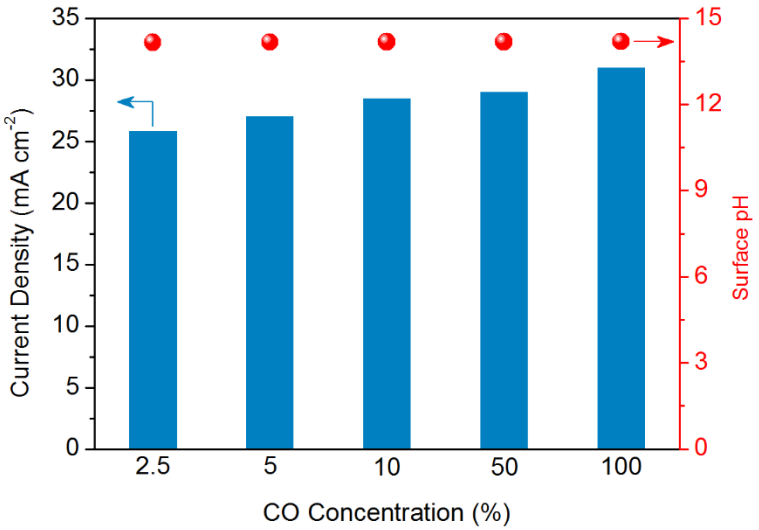

Supplementary Fig. 31. Current densities (mA cm^{-2}, left) & simulated pH at catalyst surface (right) from CORR at different CO concentrations operating at a fixed potential of -0.44 V vs. RHE in 1 M KOH.

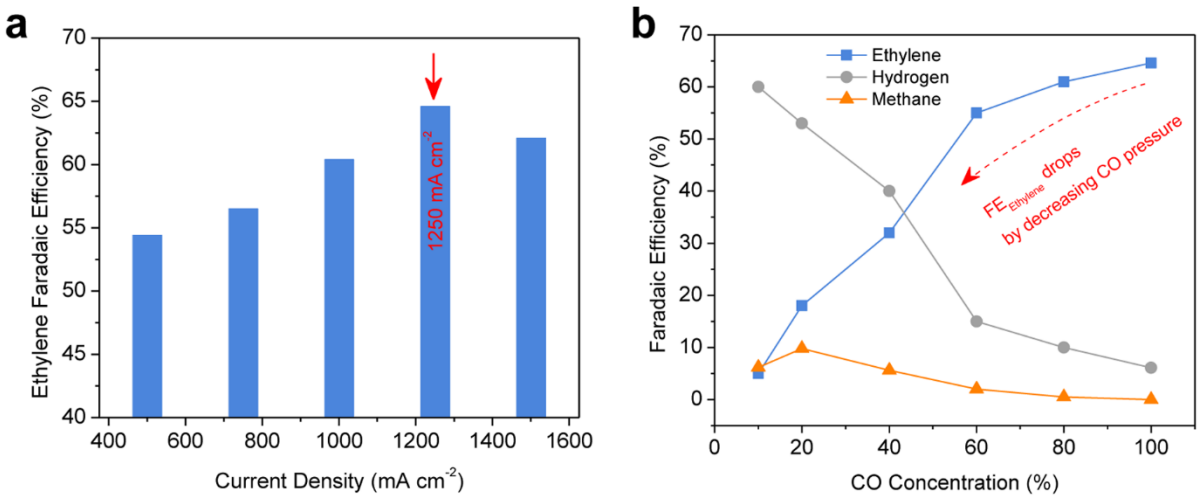

Supplementary Fig. 32. a, Ethylene Faradaic efficiency as a function of applied current density at 1 M KOH using pure CO (100%), in which $FE_{Ethylene}$ peaks at 1250 mA cm^{-2}. **b,** Faradaic efficiencies of CORR products at different CO concentrations at a constant current density of 1250 mA cm^{-2} in 1 M KOH. When CO concentration is decreased, keeping the reaction rate at the level corresponding to peak ethylene FE for 100% CO input, mass transport limitations result in lower ethylene selectivity.

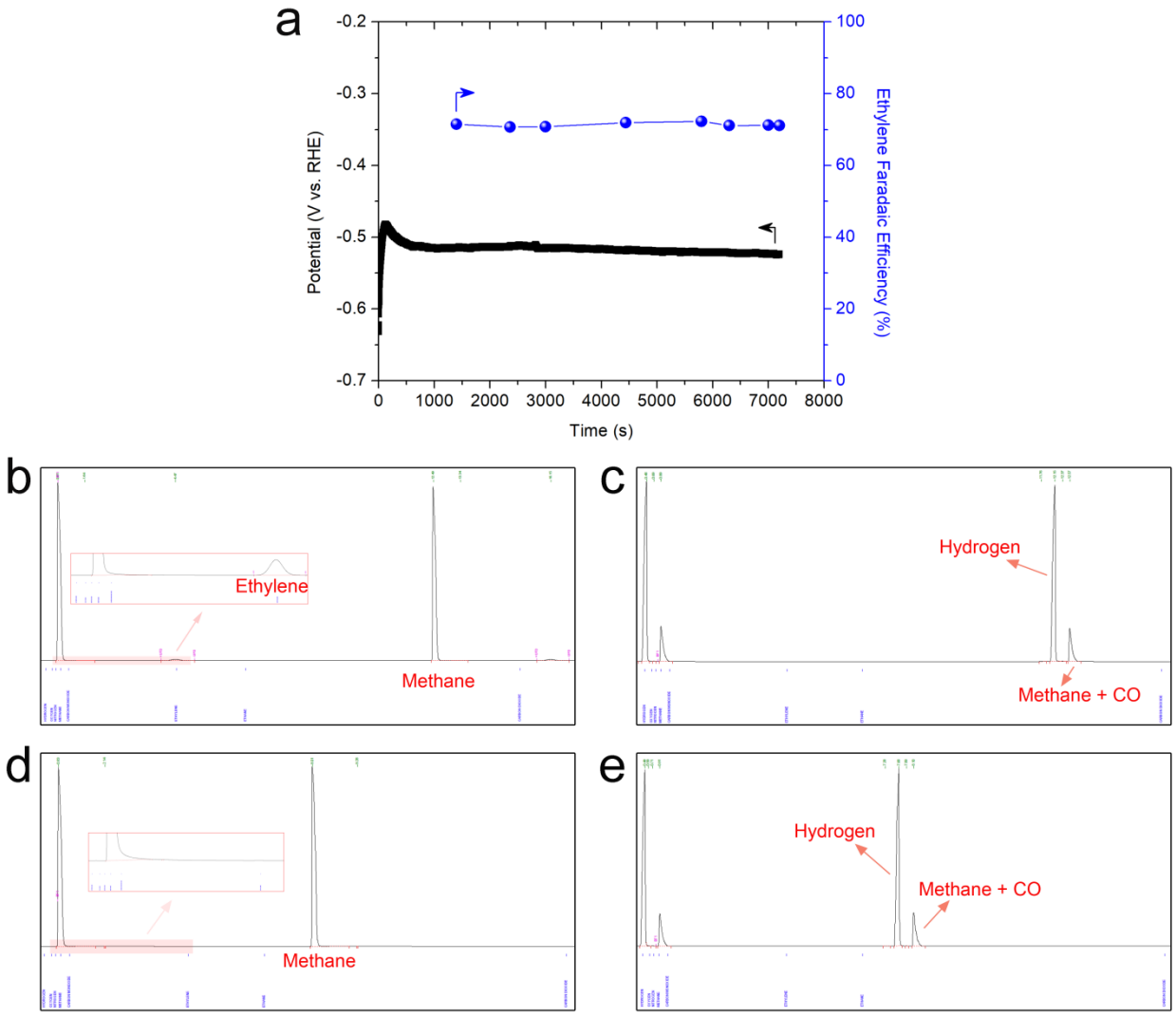

Supplementary Fig. 33. A representative CORR test using simulated coke oven gas. a. A selective ethylene production from CORR using simulated coke oven gas (10% CO + 30% CH_4 +60% H_2) in 1 M KOH at a constant current density of 150 mA cm^{-2}. **b, c,** Representative GC traces of CORR gaseous products by feeding simulated coke oven gas from FID (**b**) and TCD (**c**) channels. **d, e,** Representative GC traces of simulated coke oven gas from FID (**d**) and TCD (**e**) channels for comparison.

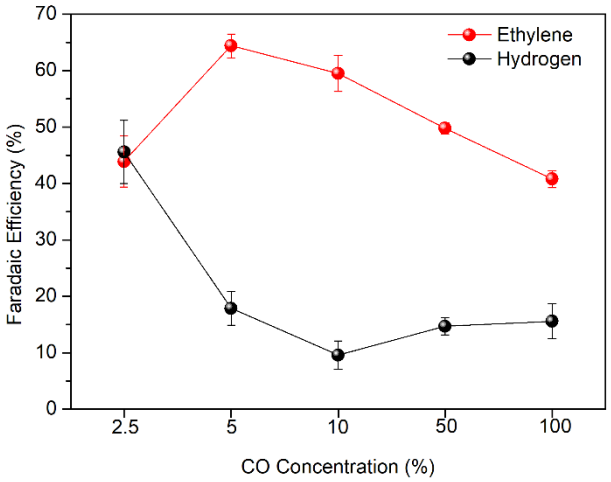

Supplementary Fig. 34. Faradaic efficiencies of CORR products at different CO concentrations at a constant current density of 120 mA cm^{-2} in 1 M KOH using commercial polycrystalline Cu (~100 nm particle size, *Sigma Aldrich*). Error bars are means ± SD (n = 3 replicates).

Supplementary Table 1. Summary of ethylene electroproduction efficiency from CO_2/CO reduction.

Catalyst	Reaction and cell type	Electrolyte	FE_{C2H4} (%)	j_{C2H4} (mA cm^{-2})	Potential (V vs. RHE)	Cathodic energy efficiency (%)
This work	**5% CORR in flow cell**	**1 M KOH**	**72**	**87**	**-0.52**	**44**
	100% CORR in flow cell	**1 M KOH**	**65**	**808**	**-0.72**	**35**
Oxide derived Cu[1]	100% CORR in flow cell	1 M KOH	44	462	-0.72	24
Copper acetate derived Cu[2]	100% CORR in H-cell using a gas diffusion electrode	10 M KOH	16	50	-0.78	8.4
Abrupt Cu interface[3]	100% CO_2RR in flow cell	10 M KOH	66	184	-0.54	44
CuAg alloy[4]	100% CO_2RR in flow cell	1 M KOH	55	172	-0.68	30
Electro-redeposited Cu[5]	100% CO_2RR in flow cell	1 M KOH	36	161	-1	17
Nanoporous Cu film[6]	100% CO_2RR in flow cell	1 M KOH	38	72	-0.6	22

Supplementary Note 1

The calculation of half-cell cathodic energy efficiency (CEE) is based on the assumption of a zero overpotential of the oxygen evolution reaction at the anode side, which is shown in equation below[3,7]:

$$CEE = \frac{(1.23+(-E_{C2H4}))*FE_{C2H4}}{1.23+(-E)} \quad (1)$$

Where E_{C2H4} = 0.17 V is the thermodynamic potential (vs. RHE) of CO reduction to ethylene (E_{C2H4} = 0.08 V for CO_2 reduction); FE_{C2H4} is the Faradaic efficiency of ethylene production; E is the applied potential vs. RHE.

Supplementary Note 2

The degree of unsaturation (DU) is defined as:

$$DU = 1 + \frac{\sum n_i(v_i - 2)}{2} \qquad (2)$$

where n_i is the number of atoms with valence v_i.

Supplementary Note 3

The volume concentration of CO and OH^- in the electrolyte was simulated using a 1D reaction-diffusion model. The governing equations:

$$\frac{\partial[CO]}{\partial t} = D_{CO}\frac{\partial^2[CO]}{\partial x^2} - R_{CO} \quad (3)$$

$$\frac{\partial[OH]}{\partial t} = D_{OH}\frac{\partial^2[OH]}{\partial x^2} - R_{OH} \quad (4)$$

were solved in COMSOL (COMSOL Multiphysics v5.3a, Stockholm, Se) using the transport of dilute species physics for a domain size of 500 μm with a 5 μm catalyst at x=0, where D_{CO} and D_{OH} are the CO and OH^- diffusivities, and R_{CO} and R_{OH} account for the CO reduction and OH^- production in the catalyst layer.

$$R_{CO} = \frac{[CO]}{[CO_{sat}]}\ \frac{j}{F}\frac{\epsilon}{L_{catalyst}}\sum\frac{FE_{CORR}}{ne_{CORR}} \quad (5)$$

$$R_{OH} = \frac{j}{F}\frac{\epsilon}{L_{catalyst}} \quad (6)$$

where $[CO_{sat}]$ is the saturation concentration of CO based on the KOH concentration (to account for Sechenov salting out effects), as well as on the temperature and partial pressure (according to Henry's law), j is the current density, F is Faraday's constant, ϵ is the porosity, FE_{CORR} is the total CORR FE, and ne_{CORR} is the number of electrons transferred per CO molecule consumed. The transport simulation assumes a uniform, porous catalyst, across which the volume concentration is determined and does not take into account pore-scale concentration variation or surface species concentration. A no flux boundary condition is applied for OH^- at x=0, and $[OH^-]$ = [KOH] at x=500 μm. For CO, a flux condition is applied at x=0 to simulate mass transfer at the gas-liquid interface:

$$\frac{\partial[CO]}{\partial x} = ka\ ([CO_{sat}] - [CO]) \quad (7)$$

where *ka* is the mass transfer coefficient (equal to 1e-4 m s^{-1}), and [CO] = 0 at x=500 μm. Simulations are time-dependent and run until steady-state occurs (~10^3 s).

Supplementary References

1 Jouny, M., Luc, W. & Jiao, F. High-rate electroreduction of carbon monoxide to multi-carbon products. *Nat. Catal.* **1**, 748-755 (2018).

2 Han, L. H., Zhou, W. & Xiang, C. X. High-rate electrochemical reduction of carbon monoxide to ethylene using Cu-nanoparticle-based gas diffusion electrodes. *ACS Energy Lett.* **3**, 855-860 (2018).

3 Dinh, C. T. *et al.* CO_2 electroreduction to ethylene via hydroxide-mediated copper catalysis at an abrupt interface. *Science* **360**, 783-787 (2018).

4 Hoang, T. T. H. *et al.* Nanoporous copper silver alloys by additive-controlled electrodeposition for the selective electroreduction of CO_2 to ethylene and ethanol. *J. Am. Chem. Soc.* **140**, 5791-5797 (2018).

5 De Luna, P. *et al.* Catalyst electro-redeposition controls morphology and oxidation state for selective carbon dioxide reduction. *Nat. Catal.* **1**, 103-110 (2018).

6 Hoang, T. T. H., Ma, S. C., Gold, J. I., Kenis, P. J. A. & Gewirth, A. A. Nanoporous copper films by additive-controlled electrodeposition: CO_2 reduction catalysis. *ACS Catal.* **7**, 3313-3321 (2017).

7 Gabardo, C. M., Seifitokaldani, A., Edwards, J. P., Dinh, C. T., Burdyny, T., Kibria, M. G., O'Brien, C. P., Sargent, E. H. & Sinton, D. Combined high alkalinity and pressurization enable efficient CO_2 electroreduction to CO. *Energy Environ.Sci.* **11**, 2531-2539 (2018).